Robust Amplitude Control Set Model Predictive Control With Low-Cost Error for SPMSM Based on Nonlinear Extended State Observer

Zhenrui Zhang, Xingyu Wang, and Jing Xu

***Abstract*—The finite control set model predictive current control involves addressing challenges related to greater cost function values and inaccurate current prediction models, which can adversely impact the steady-state performance in permanent magnet synchronous motor (PMSM). A robust amplitude control set model predictive current control method (RACSMPCC) is proposed in this study, aiming to enhance prediction accuracy and control precision. This method introduces a rotation coordinate system amplitude control set to reduce the cost function value and improve current control precision. Then, a nonlinear extended state observer (NESO) is employed to observe and compensate for comprehensive disturbances in the current prediction equation, thereby improving the accuracy of the current prediction. Simultaneously, a parameter configuration method in the complex frequency domain is proposed for NESO, and its influence on the disturbance rejection performance of the system is analyzed. Hardware experiments on a PMSM are conducted to validate the effectiveness of RACSMPCC in reducing cost function and improving current control accuracy.**

***Index Terms*—Current harmonic suppression, finite control set model predictive current control, nonlinear extended state observer, permanent magnet synchronous motor (PMSM).**

I. Introduction

IN RECENT years, industrial servomechanism has witnessed the application of various drive control strategies and motors with superior performance, thanks to the rapid development of power electronics technology [1], [2], [3]. Vector control exhibits good comprehensive performance but requires parameter tuning [4]. The dynamic performance of direct torque control is superior, but the problem of torque ripple restricts its development [5]. Finite control set model predictive current control (FCSMPCC) has the potential to realize system multiobjective optimization. Therefore, it has received extensive attention. Such methods can be divided into direct speed control [6], torque control [7], and current control [8]. On this basis, it can optimize the performance of the drive system in many aspects, such as maximum torque per ampere [7], flux weakening control [9], and dc-link oscillation suppression [10]. FCSMPCC usually is used to solve multiobjective optimization, but its steady-state performance is often unsatisfactory. The FCSMPCC usually designs the control set based on the inverter state. The two-level voltage source inverter, as an example, uses six effective voltage vectors that the inverter can output to control the motor. Because the six voltage vectors are scattered in a circle space, the optimal predicted vector may have considerable prediction errors compared to the required vector for the motor, leading to harmonic currents and mechanical noise [11]. The prediction deviation is also directly related to the change in motor parameters. An inaccurate mathematical model will also cause significant current harmonics and torque ripple, affecting the system's stable operation [12].

The optimal vector's amplitude error can be minimized by controlling the output vector's switching time, thereby mitigating the current harmonics resulting from voltage vector discrepancies. In [13], the optimal scheme is given under different motor states to reduce the flux harmonic. Two feasible vector combinations are considered in [14] and [15] to calculate the corresponding duty cycle to compute the control vector. Nevertheless, the duty cycle computation depends on the mathematical model and motor parameters. Inaccurate parameters can compromise the robustness of the control approach and hinder the optimization of multiple control objectives. In addition, the optimization of the cost function design can also contribute to the reduction of current harmonics [16]. However, it cannot solve the current harmonic caused by a significant prediction error. Expanding the virtual vector control set can also reduce the cost function. In [17], the amplitude of the basic voltage vectors is divided into three segments and develops into 18 voltage vectors. Like this method, in [18], the amplitude of six effective primary vectors is reduced to one-half of the original and synthesizes two adjacent voltage vectors into a new vector. In [19], virtual vectors with different phase angles are generated by evenly dividing adjacent primary effective vectors included angles to construct extended vector sets. Based on the virtual voltage vector scheme synthesized by three active vectors, harmonic

Manuscript received 25 September 2023; revised 8 January 2024 and 23 February 2024; accepted 18 March 2024. Date of publication 22 March 2024; date of current version 19 April 2024. This work was supported in part by the National Natural Science Foundation of China under Grant 51979021 and Grant 51905229, in part by the JUST Doctoral Research Startup Funding under Grant 1172932302, and in part by Jiangsu University (High-tech Ships) Collaborative Innovation Center Project under Grant XTCXKY20230002. Recommended for publication by Associate Editor S.-C. Yang. *(Corresponding authors: Zhenrui Zhang; Jing Xu.)*

The authors are with the Department of Marine Equipment and Technology Institute, Jiangsu University of Science and Technology, Zhenjiang 212003, China (e-mail: tabz00@just.edu.cn; 202200000212@just.edu.cn; xujing@just.edu.cn).

Color versions of one or more figures in this article are available at https://doi.org/10.1109/TPEL.2024.3380577.

Digital Object Identifier 10.1109/TPEL.2024.3380577

voltage components are eliminated in [20]. These methods increase the number of voltage vectors in the rotating coordinate system so that each control cycle will enhance the coordinate transformation computation. These methods still cannot avoid the vector phase error. Therefore, designing the control set in a rotating coordinate system is more meaningful. However, few reports exist on creating amplitude control sets in the rotating coordinate system.

When there are few voltage vectors in the optimization process, the system still has strong robustness even if the motor parameters change significantly. However, if the motor parameters change, the output control value from the extended control set may no longer be optimal. Therefore, reducing the influence of time-varying motor parameters on model predictive control is necessary. Online motor parameter identification can obtain accurate motor parameters in real-time [21]. However, this method has an extensive calculation and fails to address the issue of inaccurate modeling. The feedforward compensation strategy directly using the current prediction difference is a direct compensation method [22], [23], [24]. Although the current prediction values obtained by all voltage vectors in each control cycle are compensated and corrected, the prediction error update corresponding to each voltage vector is delayed, reducing compensation effectiveness during dynamic processes. In addition, disturbance observers help to improve the antidisturbance performance of the system, such as the Luenberger observer [25], extended Kalman filter [26], sliding mode observer [27], and adaptive observer [28]. Compared with the motor parameter identification scheme and the prediction compensation method, the disturbance observation compensation scheme can consider more influencing factors simultaneously and has relatively low requirements for microprocessor performance [29]. Han [30] proposed the active disturbance rejection control technology, in which the extended state observer can effectively reduce the impact of inaccurate mathematical modeling on the controller. By reforming the mathematical model, the easily disturbed part of the motor model is extended to an independent state variable and observed. Based on this method, progress has also been made in reducing the model prediction error. A model-free predictive control method based on the linear observer is proposed in [30] and [31]. However, this method is based on the deadbeat model predictive control, which is not conducive to the multiobjective optimization of the control object. In the present research results, the disturbance compensation structure for the permanent magnet synchronous motor (PMSM) multiobjective optimal predictive control scheme is still relatively rare, and the control structure in this article enriches this deficiency.

This article proposes robust amplitude control set model predictive current control method (RACSMPCC) to improve the control and predictive accuracy of FCSMPCC, which enhances the steady-state and dynamic performance of the system. The main contributions are twofold.

First, a design approach for the amplitude control set is proposed to improve control accuracy. This control set is designed based on the motor voltage equation in the rotating coordinate system, avoiding the need for coordinate transformation computation. The phase angle error is also eliminated by synthesizing the control vector based on the rotor position to improve the *dq*-axis current control performance.

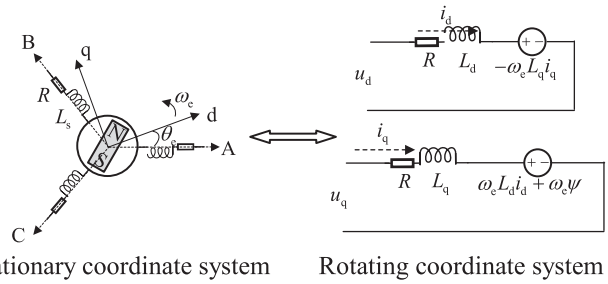

Fig. 1. Diagram of the PMSM's equivalent structure circuit.

Second, the predictive model is simplified using an ultralocal model, and a corresponding nonlinear extended state observer (NESO) is designed to observe the disturbances of the predictive model. Furthermore, a bandwidth-based NESO parameter configuration method is introduced, and experimental comparisons are conducted with other observers to demonstrate the advantages of the observer in terms of parameter configuration. The impact of NESO on system disturbances is analyzed through Bode plots.

The performance of the control method proposed in this article is verified through experimental analysis. The rest of this article organized as follows. Section II introduces the mathematical model of the motor and proposes a design method for voltage amplitude control. Section III presents a disturbance suppression method based on NESO, where the observer is linearized and treated as a second-order low-pass filter to simplify the application of the nonlinear function. An overdamping parameter configuration method is proposed to ensure system stability. Furthermore, the impact of NESO on the system's disturbance rejection performance is analyzed using an equivalent control structure. In Section IV, an experimental setup is established to validate the performance of RACSMPCC by comparing it with other methods. Finally, Section V concludes this article.

II. Amplitude Control Set Model Predictive Control Strategy

This section introduces the PMSM mathematical model. Subsequently, the amplitude control set model predictive current control method (ACSMPCC) is proposed to reduce the predictive errors of FCSMPCC. In addition, prediction errors between the two methods are compared within a single control cycle.

A. Mathematical Model of PMSM

As illustrated in Fig. 1, the schematic diagram displays the permanent magnet synchronous motor equivalent circuit structure. The inductance values along the *dq*-axis are equal for surface-mount PMSMs (SPMSM): $L_{\mathrm{d}} = L_{\mathrm{q}} = L_{\mathrm{s}}$. The *dq*-axis current model of the motor in a rotating coordinate

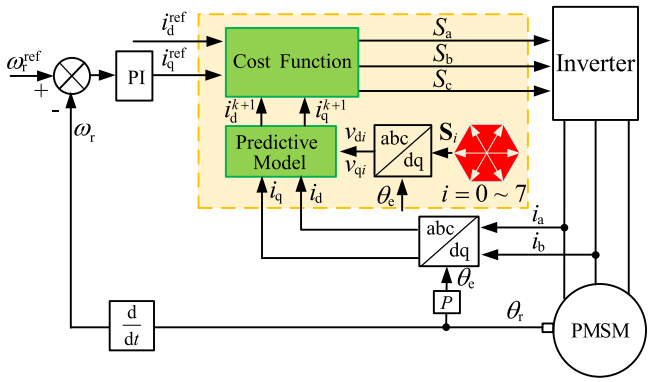

Fig. 2. FCSMPCC control structure.

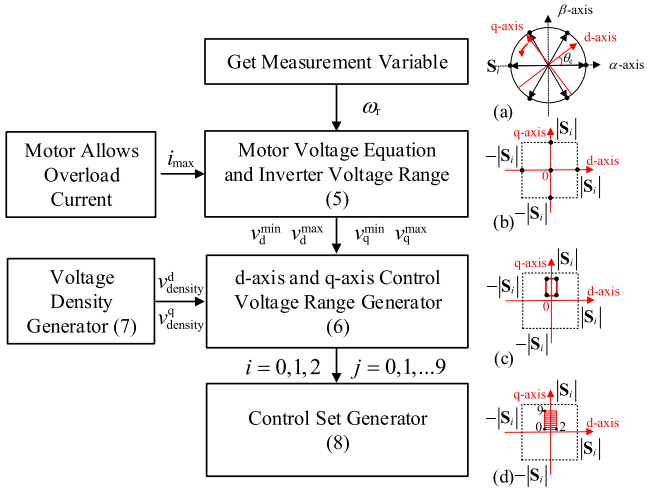

Fig. 3. Amplitude control set design process.

system is as

$$\begin{cases} \frac{\mathrm{d}i_\mathrm{d}}{\mathrm{d}t} = -\frac{R_\mathrm{s}}{L_\mathrm{d}} i_\mathrm{d} + \frac{L_\mathrm{q}}{L_\mathrm{d}} \omega_\mathrm{e} i_\mathrm{q} + \frac{1}{L_\mathrm{d}} v_\mathrm{d} \\ \frac{\mathrm{d}i_\mathrm{q}}{\mathrm{d}t} = -\frac{R_\mathrm{s}}{L_\mathrm{q}} i_\mathrm{q} - \frac{L_\mathrm{d}}{L_\mathrm{q}} \omega_\mathrm{e} i_\mathrm{d} - \omega_\mathrm{e} \frac{\psi}{L_\mathrm{q}} + \frac{1}{L_\mathrm{q}} v_\mathrm{q} \end{cases} \tag{1}$$

where, i_d, i_q and v_d, v_q are the motor dq-axis current and voltage. ω_e, R_s, and ψ are the motor electrical angular velocity, winding resistance, and permanent magnet flux linkage, respectively.

Assuming that the sampling period is T_s, the forward Euler method is used to discretize (1) to obtain the current prediction equation of PMSM as

$$\begin{aligned} i_\mathrm{d}^{k+1} &= i_\mathrm{d}^k + \frac{T_\mathrm{s}}{L_\mathrm{d}} \left(v_\mathrm{d}^k - R i_\mathrm{d}^k + \omega_\mathrm{e}^k L_\mathrm{q} i_\mathrm{q}^k \right) \\ i_\mathrm{q}^{k+1} &= i_\mathrm{q}^k + \frac{T_\mathrm{s}}{L_\mathrm{q}} \left(v_\mathrm{q}^k - R i_\mathrm{q}^k - \omega_\mathrm{e}^k L_\mathrm{d} i_\mathrm{d}^k - \psi \omega_\mathrm{e}^k \right) \end{aligned} \tag{2}$$

where k represents the current sampling period, and $k+1$ is the predictive current. v_q^k and v_d^k are the control solutions in the rotating coordinate system. Predicting the current values at $k+1$ for all basic voltage vectors by the FCSMPCC through calculating (2) [7]. Subsequently, the cost values of all basic voltage vectors can be determined by

$$J_\mathrm{MPCC} = \left(i_\mathrm{d}^\mathrm{ref} - i_\mathrm{d}^{k+1} \right)^2 + \left(i_\mathrm{q}^\mathrm{ref} - i_\mathrm{q}^{k+1} \right)^2 + J_\mathrm{limit} \tag{3}$$

where i_q^ref is the q-axis reference current output by the speed loop and J_limit represents the current constraint [6].

Fig. 2 depicts the control structure of FCSMPCC, which involves three steps. First, the dq-axis current reference value is determined based on the speed loop. The basic voltage vector is then transformed into the dq-axis coordinate system based on the rotor position. Subsequently, each vector's predictive dq-axis current values are predicted and taken into the cost function to evaluate the optimum voltage vector. Finally, the inverter is switched accordingly to apply the chosen voltage vector to the motor.

The FCSMPCC's main issue lies in the eight space voltage vectors distributing 360°, causing a significant phase and amplitude difference. Hence, during the prediction process, it is challenging to consistently select the optimal vector that aligns with the desired reference vector, resulting in significant current harmonics in the motor current due to large prediction errors. Increasing the virtual space voltages in the stationary coordinate system puts excessive pressure on the controller. Therefore, this article directly designs the voltage amplitude control set in the rotating coordinate system, reducing the range of amplitude selection and saving calculation efforts related to coordinate transformation.

B. Amplitude Control Set Design Method

The control set in FCSMPCC comprises eight basic voltage vectors, as shown in Fig. 3(a). The control set is in the stationary reference frame, but the control implementation of the motor is usually in the d-q rotating reference frame. Therefore, the control set in the stationary reference frame must undergo coordinate transformation to predict the motor current. In addition, there may be phase errors present. The amplitude control set in a rotating coordinate system can be designed to avoid those problems based on the amplitude $|\mathbf{S}_i|$ of the basic voltage vectors, as shown in Fig. 3(b). The basic voltage amplitude control set is formed in

$$\{(0,0), (0, |\mathbf{S}_i|), (0, -|\mathbf{S}_i|), (|\mathbf{S}_i|, |\mathbf{S}_i|), (-|\mathbf{S}_i|, -|\mathbf{S}_i|)\}. \tag{4}$$

Compared to the basic vector control set, the amplitude control set (4) does not require coordinate transformation for each vector and has fewer numbers. The amplitude control set has a distinct advantage regarding computational performance but does not significantly improve control accuracy. Therefore, it is necessary to adopt specific optimization mechanisms to improve the control accuracy of the control set. At this point, there are two approaches. The first approach is to manually divide the control region depicted in Fig. 3(b) [composed by (4)] to generate more control solutions. This control set includes all possible voltage vectors of the inverter, regardless of the motor's state. Although this approach can enhance the control performance of specialized motors, it comes at the cost of sacrificing control accuracy and computational efficiency. The voltage equation designs the other approach. The voltage equation of the motor

in the rotating coordinate system is as

$$v_{\mathrm{d}} = L_{\mathrm{d}}\frac{\mathrm{d}i_{\mathrm{d}}}{\mathrm{d}t} + R_{\mathrm{s}}i_{\mathrm{d}} - \omega_{\mathrm{e}}L_{\mathrm{q}}i_{\mathrm{q}}$$
$$v_{\mathrm{q}} = L_{\mathrm{q}}\frac{\mathrm{d}i_{\mathrm{q}}}{\mathrm{d}t} + R_{\mathrm{s}}i_{\mathrm{q}} + \omega_{\mathrm{e}}L_{\mathrm{d}}i_{\mathrm{d}} + \psi\omega_{\mathrm{e}}. \tag{5}$$

Due to the motor's inductance and direct current variations in (5), it can be inferred that the magnitude of the current does not undergo significant changes within a given sampling time. Therefore, compared to the back electromotive force, the product of inductance and the differential term of current can be neglected. In addition, constraining current variations is necessary to prevent excessive fluctuations of torque. Instead, the voltage range can be designed using the maximum allowable current, usually around 3–5 times the rated current. The SPMSM exhibits 0 for the *d*-axis current reference value. Therefore, when designing the *d*-axis voltage, only the *q*-axis current and speed terms must be considered for SPMSM. Similarly, for the *q*-axis voltage, after disregarding the differential term and *d*-axis current term, only the *q*-axis current and speed terms need to be taken into account. Although this article primarily focuses on the SPMSM, an amplitude control set can also be designed for the interior PMSM by calculating the *d*-axis current.

The reference value for the control set is determined by selecting the larger value between current and speed in order to minimize the control set's range. Consequently, the current is utilized as the range value for designing the voltage range at a specific speed. The load torque mainly determines the motor current. The voltage range can be estimated based on the motor's permissible maximum output torque. For example, the electrical angular speed is ω_{e}. The motor's maximum current is $i_{\max}$, and the voltage range in the rotating coordinate system is as follows:

$$v_{\mathrm{d}}^{\min} = -\omega_{\mathrm{e}}L_{\mathrm{q}}i_{\max} \le v_{\mathrm{d}} \le v_{\mathrm{d}}^{\max} = \omega_{\mathrm{e}}L_{\mathrm{q}}i_{\max}$$
$$v_{\mathrm{q}}^{\min} = \psi\omega_{\mathrm{e}} - R_{\mathrm{s}}i_{\max} \le v_{\mathrm{q}} \le v_{\mathrm{q}}^{\max} = R_{\mathrm{s}}i_{\max} + \psi\omega_{\mathrm{e}}. \tag{6}$$

The amplitude control region for a particular motor state can be selected according to (6), as shown in Fig. 3(c). The voltage density of the *d*-axis and *q*-axis voltages is determined for this region based on the number of iterations that the actual processor can perform

$$v_{\mathrm{density}}^{\mathrm{d}} = \frac{v_{\mathrm{d}}^{\max} - v_{\mathrm{d}}^{\min}}{N_{\mathrm{d}}}, v_{\mathrm{density}}^{\mathrm{q}} = \frac{v_{\mathrm{q}}^{\max} - v_{\mathrm{q}}^{\min}}{N_{\mathrm{q}}} \tag{7}$$

where N_{d} and N_{q} are the number of partitions in the voltage range. The selection of N_{d} and N_{q} is related to the controller's performance. Then, the control set can be defined as

$$\{(v_{\mathrm{d}}^{\min} + iv_{\mathrm{density}}^{\mathrm{d}}, v_{\mathrm{q}}^{\min} + jv_{\mathrm{density}}^{\mathrm{q}})_{i=0\sim N_{\mathrm{d}}, j=0\sim N_{\mathrm{q}}}\}. \tag{8}$$

The voltage range involved in *d*-axis voltage is small, so N_{d} can be set smaller. The voltage range involved in *q*-axis voltage is extensive, so its voltage selection density can be slightly greater.

The process of generating the amplitude control set, as shown in Fig. 3, begins with measuring the motor speed, determining the inverter voltage vectors [see Fig. 3(a)], and establishing the range of the inverter amplitude [see Fig. 3(b)]. Next, the voltage selection range [see Fig. 3(c)] for the *d*-axis and *q*-axis is determined based on the maximum allowable current of the motor. Subsequently, the voltage range [see Fig. 3(d)] is manually partitioned according to the voltage density or number of partitions, generating the amplitude control set (8).

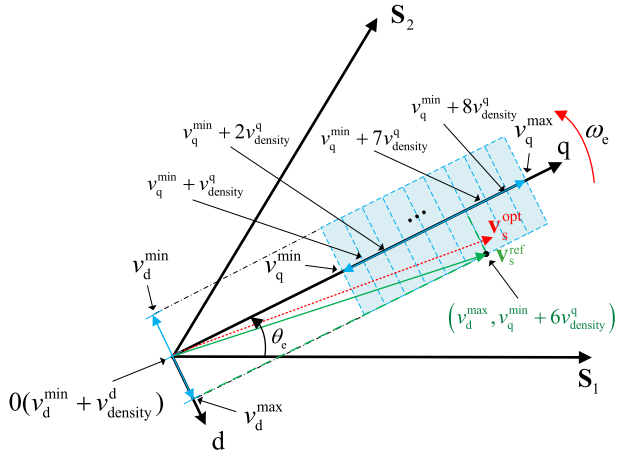

Fig. 4. Control set selection principle of ACSMPCC.

The prediction equations and cost functions typically determine the optimal voltage vector. During the control process of the motor, the voltage vector should scan through a continuous circular shape, meaning that the optimal vector can appear at any position. Fig. 4 analyzes a specific case in the first sector. Let $\mathbf{v_s^{opt}}$ denote the ideal voltage vector of the motor in a specific control state. The role of model predictive control is to accurately evaluate this vector using prediction equations and cost functions and select a vector from the control set to approximate it. It can be observed that FCSMPCC will choose vector $\mathbf{S}_2$ or $\mathbf{S}_1$ to approximate the optimal vector, resulting in a significant deviation from the optimal vector. ACSMPCC will form a vector control region in the *dq*-axis coordinate system, and each solution in the control region has a lower deviation. According to the motor speed, the control region (blue part) of $v_{\mathrm{q}}^{\min}$, $v_{\mathrm{q}}^{\max}$, $v_{\mathrm{d}}^{\min}$, and $v_{\mathrm{d}}^{\max}$ can be determined by (6). Next, the control subset of the control region is determined based on (8). Finally, the control solution closest to the optimal vector can be obtained by iterating through the control set.

C. Prediction Error Analysis of FCSMPCC and ACSMPCC

Fig. 5(a) and (b) shows the two possible optimal vectors in the first sector. Each voltage vector corresponds to voltage control solutions ($\mathbf{v_{s1}}$, $\mathbf{v_{s2}}$, and $\mathbf{v_{s3}}$) approximated by FCSMPCC, duty-cycle FCSMPCC, and ACSMPCC. δ_1, δ_2, and δ_3 are the errors between the three methods' selected vector and the optimal vector.

Among the three methods considered for selection, the FCSMPCC exhibits the largest deviation between the predicted voltage vector and the optimal vector, followed by the duty cycle FCSMPCC. At the same time, the ACSMPCC shows the smallest error. ACSMPCC is achieved by selecting the voltage value in the rotating coordinate system, which reduces phase errors. Moreover, designing the magnitude control set based on

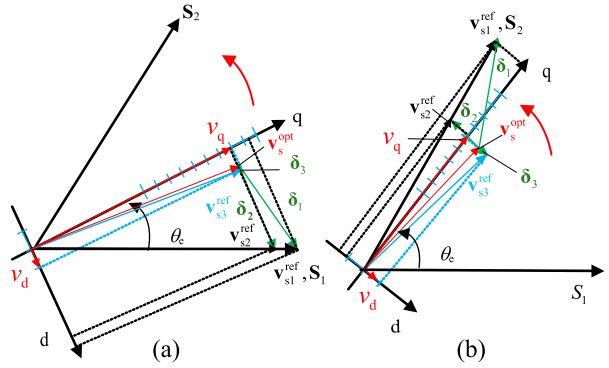

Fig. 5. Error analysis of ACSMPCC and FCSMPCC in different control vectors.

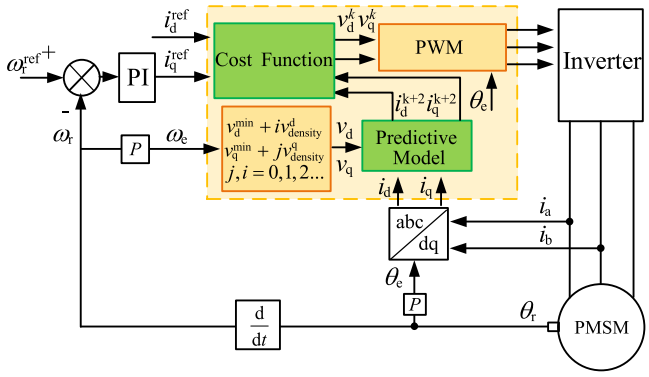

Fig. 6. ACSMPCC control structure.

the motor voltage equation is beneficial in reducing magnitude errors.

D. Control Structure of ACSMPCC

ACSMPCC's system control structure diagram is similar to that of FCSMPCC, as shown in Fig. 6. The speed loop calculates the q-axis reference current, and the d-axis reference current of surface-mounted PMSM is set to 0. During the computation of the optimal solution, the maximum values of v_{d} and v_{q} for the control set are obtained separately using (6). Then, the voltage iteration step size, such as N_{d} and N_{q}, is determined in (7). For example, if the d-axis is divided into three parts, N_{d} is set to two. Similarly, if the q-axis is divided into ten parts, N_{q} is set to nine. The combination of v_{d} and v_{q} forms the 30 control sets (v_{d}, v_{q}), as depicted in (8). Subsequently, each of these 30 subsets is evaluated by substituting them into (2) and (3), resulting in the computation of 30 cost function values. A control subset $(v_{\mathrm{d}}^{k}, v_{\mathrm{q}}^{k})$ corresponding to the minimum cost function value is selected as the optimal voltage solution.

As mentioned above, the optimal control voltage vector of the motor is determined by accurate prediction equations and cost functions. However, if there is a deviation in the prediction equations, the obtained optimal control solution may differ from the actual optimal control solution. Therefore, in addition to improving the control accuracy of the control set, it is also necessary to enhance the accuracy of the prediction model.

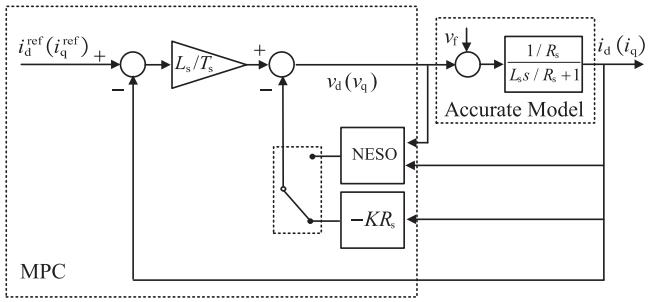

Fig. 7. Equivalent control structure of RACSMPCC.

III. Robust Amplitude Model Predictive Control Based on Nonlinear Extended State Observer

In the previous section, although the ACSMPCC reduces the cost function value. The optimal vector selection is only achieved when the prediction model is consistent with the actual motor model. Any changes in motor parameters or deviations in the prediction model (2) can result in suboptimal control solutions, disrupting system steady-state performance, and the presence of noticeable steady-state current harmonics.

Assuming parameter deviations and current disturbances exist in the motor equation. "△" represents the parameter error between the prediction and the actual motor. The accurate motor current mathematical can be represented by

$$\begin{cases} \frac{\mathrm{d}i_{\mathrm{d}}}{\mathrm{d}t} = -\frac{R_{\mathrm{s}}+\triangle R_{\mathrm{s}}}{L_{\mathrm{s}}+\triangle L_{\mathrm{s}}} i_{\mathrm{d}} + \frac{1}{L_{\mathrm{s}}+\triangle L_{\mathrm{s}}} v_{\mathrm{d}} + \omega_{\mathrm{e}} i_{\mathrm{q}} \\ \frac{\mathrm{d}i_{\mathrm{q}}}{\mathrm{d}t} = -\frac{R_{\mathrm{s}}+\triangle R_{\mathrm{s}}}{L_{\mathrm{s}}+\triangle L_{\mathrm{s}}} i_{\mathrm{q}} + \frac{1}{L_{\mathrm{s}}+\triangle L_{\mathrm{s}}} v_{\mathrm{q}} - \omega_{\mathrm{e}} i_{\mathrm{d}} - \omega_{\mathrm{e}} \frac{\psi+\triangle\psi}{L_{\mathrm{s}}+\triangle L_{\mathrm{s}}}. \end{cases} \tag{9}$$

First, the influence of speed on the inner current loop is disregarded to analyze the impact of parameter transformation on the current loop. By assuming an approximate cost function of zero, the control structure diagram is shown in Fig. 7, based on the analysis of FCSMPCC discussed in [33 Chapter 6]. Assuming v_{f} represents the equivalent voltage disturbance. The closed-loop transfer function between the reference and output current values is as

$$\frac{i_{\mathrm{q}}(s)}{i_{\mathrm{q}}^{\mathrm{ref}}(s)} = \frac{1}{T_s s + \underbrace{1 + (R_s T_s - K R_s T_s)/L_{\mathrm{s}}}_{K'}}, K > 0 \tag{10}$$

where K represents the deviation between the actual parameters and the control parameters. In the following analysis, variables in the complex frequency domain are represented by adding (s), while the rest are all time-domain models.

It can be observed in (10) that when $K' < 0$, the system exhibits a right-half plane pole. As shown in Fig. 8(a), the value of K impacts the system's steady-state control accuracy. It can be deduced from the closed-loop transfer function of the current loop that only when $K = 1$ can the system achieve zero-error control. The excessive gain increases the steady-state control error, which is detrimental to the stable control of the system.

Furthermore, the impact of different K values on the speed loop can be analyzed. The transfer function of the speed loop PI controller is

$$\mathrm{PI(s)} = K_{\mathrm{p}} + \frac{K_{\mathrm{i}}}{s}. \tag{11}$$

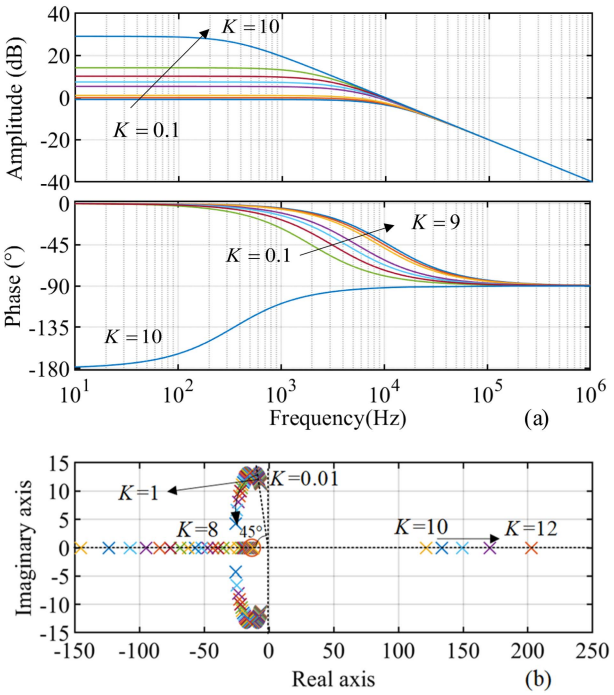

Fig. 8. Steady-state performance and stability analysis of ACSMPCC. (a) Bode plot of the current closed-loop transfer function with different *K*. (b) Motor speed's root locus diagram changes as *K*.

The transfer function of the motor motion equation is

$$\frac{\omega_{\mathrm{r}}(s)}{i_{\mathrm{q}}(s)} = \frac{1.5P\psi}{J}. \tag{12}$$

Combined with the transfer function of the inner current loop, the motor system's transfer function is shown in

$$\begin{aligned}
\frac{\omega_{\mathrm{r}}^{\mathrm{ref}}(s)}{\omega_{\mathrm{r}}(s)} &= \frac{(-1.5P\psi L_{\mathrm{s}}K_{\mathrm{p}})\ s - 1.5K_{\mathrm{i}}P\psi L_{\mathrm{s}}}{m_3 s^3 + m_2 s^2 + m_1\, s + m_0} \\
m_3 &= -JL_{\mathrm{s}}T_{\mathrm{s}} \\
m_2 &= JKR_{\mathrm{s}}T_{\mathrm{s}} - JR_{\mathrm{s}}T_{\mathrm{s}} - JL_{\mathrm{s}} \\
m_1 &= -1.5P\psi L_{\mathrm{s}}P_{\mathrm{s}} \\
m_0 &= -1.5K_{\mathrm{i}}P\psi L_{\mathrm{s}}
\end{aligned} \tag{13}$$

where $K_{\mathrm{p}} = 0.089$, $K_{\mathrm{i}} = 1.1744$.

From Fig. 8(b), it can be observed that as *K* increases, the root locus of the system moves to the left and then to the right, eventually leading to system instability. This indicates an improvement in dynamic performance, with the dominant poles moving closer to the left. However, only when *K* equals one does the dominant pole's damping coefficient approach 0.707, close to an ideal control system. When *K* exceeds 10, the system stability leads to instability. Moreover, the disturbance rejection capability gradually deteriorates.

The variation of *K* has a bad influence on the current loop's steady-state performance and the speed loop's dynamic performance. Inaccurate values of *K* can lead to steady-state errors in the current loop, and in severe cases, it can disrupt the system's stability. Moreover, if there are disturbances in the system, the inaccurate value of *K* can also affect the disturbance rejection capability. Therefore, it is essential to construct an accurate predictive model for control systems.

A. Current Disturbance Nonlinear Extended Observer

The current model is divided into the input and lumped disturbance parts to simplify the analysis. Then, the mathematical model (9) can be represented by an ultralocal model ignoring motor parameters [31]

$$\begin{cases}
\dot{\mathbf{i}}_{\mathrm{s}} = \mathbf{I}_{\mathrm{f}} + b\mathbf{v}_{\mathrm{s}} \\
\dot{\mathbf{I}}_{\mathrm{f}} = \mathbf{w}(t) \\
\mathbf{y} = \mathbf{i}_{\mathrm{s}}
\end{cases} \tag{14}$$

where $\mathbf{i_s} = [i_{\mathrm{d}}, i_{\mathrm{q}}]^{\mathrm{T}}, \mathbf{v}_{\mathrm{s}} = [v_{\mathrm{d}}, v_{\mathrm{q}}]^{\mathrm{T}}, \mathbf{I}_{\mathrm{f}} = [i_{\mathrm{df}}, i_{\mathrm{qf}}]^{\mathrm{T}}$. b is the gain of the input value, and $\mathbf{I}_{\mathrm{f}}$ is a nonlinear current disturbance term that replaces all disturbance terms, and i_{df} and i_{qf} replace model disturbances in the current

$$\mathbf{I}_{\mathrm{f}} = \begin{bmatrix} f_{\mathrm{d}} - \frac{R+\Delta R}{L_{\mathrm{s}}+\Delta L_{\mathrm{s}}} i_{\mathrm{d}} + \omega_{\mathrm{e}} i_{\mathrm{q}}, \\ f_{\mathrm{q}} - \frac{R+\Delta R}{L_{\mathrm{s}}+\Delta L_{\mathrm{s}}} i_{\mathrm{q}} - \omega_{\mathrm{e}} i_{\mathrm{d}} - \omega_{\mathrm{e}} \frac{\psi_{\mathrm{f}}+\Delta\psi_{\mathrm{f}}}{L_{\mathrm{s}}+\Delta L_{\mathrm{s}}} \end{bmatrix}.$$

The state current $\mathbf{I}_{\mathrm{f}}$ of the motor is a nonlinear disturbance. According to Prof. Han's ESO design theory [34], a nonlinear function is used to construct a second-order NESO

$$\begin{cases}
\mathbf{e}_1 = \mathbf{z}_1 - \mathbf{i}_{\mathrm{s}} \\
\dot{\mathbf{z}}_1 = \mathbf{z}_2 - \beta_1 \mathbf{e}_1 + b\mathbf{v}_s \\
\dot{\mathbf{z}}_2 = -\beta_2 \mathrm{fal}(\mathbf{e}_1, \alpha, \delta) \\
\hat{\mathbf{y}} = \mathbf{z_1}
\end{cases} \tag{15}$$

where $\mathbf{z}_1$ is the observed value of *dq*-axis current. $\mathbf{z}_2$ is the observed value of the PMSM control system state current $\mathbf{I}_{\mathrm{f}}$, and $\mathbf{e_1}$ is the observation error. The nonlinear fal function is as follows:

$$\mathrm{fal}(e, \alpha, \delta) = \begin{cases} \frac{e}{\delta^{1-\alpha}}, & |e| \leqslant \delta \\ |e|^{\alpha}\mathrm{sign}(e), & |e| > \delta \end{cases}. \tag{16}$$

α and δ are the adjustable parameters of the nonlinear function. The value range of α is generally $0 \sim 1$. The smaller its value is, the stronger the nonlinearity of the fal function is; δ is the filtering parameter of NESO. The detailed selection criteria have been provided in [34] and [30] and will not be reiterated here. The system can estimate the state variable and the lumped disturbance if the parameters are appropriately selected.

The following results can be obtained when the system enters the steady state:

$$\begin{cases}
\mathbf{e}_1 = \mathbf{z}_1 - \mathbf{i}_{\mathrm{s}}, \mathbf{e}_2 = \mathbf{z}_2 - \mathbf{I}_{\mathrm{f}} \\
\dot{\mathbf{e}}_1 = \mathbf{e}_2 - \beta_1 \mathbf{e}_1 \\
\dot{\mathbf{e}}_2 = \mathbf{w}(t) - \beta_2 \mathrm{fal}\left(\mathbf{e}_1, 0.5, 0.01\right).
\end{cases} \tag{17}$$

The parameters in (17) are designed as $\alpha = 0.5$, $\delta = 0.01$ to suppress chattering and ensure stability [35]. Then, considering the measurement noise, the corresponding steady-state error of the steady-state system is

$$\begin{cases}
\mathbf{e}_1 = \mathbf{z}_1 - \mathbf{i}_{\mathrm{s}} = \left(\frac{\mathbf{w}(t)}{\beta_2}\right)^2 \\
\mathbf{e}_2 = \mathbf{z}_2 - \mathbf{I}_{\mathrm{f}} = \beta_1 \left(\frac{\mathbf{w}(t)}{\beta_2}\right)^2.
\end{cases} \tag{18}$$

When $\beta_2 \gg \mathbf{w}(t)$, the steady-state error magnitude of the NESO is small. Therefore, the fal function can improve the convergence speed of the system, and the steady-state observation effect is also much better.

B. NESO Parameter Configuration

Since observing the d-axis current is consistent with the q-axis in (10), i_q (or i_d) is used to simplify the analysis. $\hat{i}_\mathrm{q}$ (or $\hat{i}_\mathrm{qf}$) and $\hat{i}_\mathrm{qf}$ (or $\hat{i}_\mathrm{df}$) are the corresponding observation value and disturbance term, and e_q is used to replace the observation error of the corresponding q-axis (or d-axis). At the same time, to more conveniently analyze the NESO in (15), abounded variable function f is set by

$$f = \frac{fal\,(e,\alpha,\delta)}{e} = \begin{cases} \delta^{\alpha-1}, & |e| \leqslant \delta \\ |e|^{\alpha-1}, & |e| > \delta \end{cases}. \tag{19}$$

Take the q-axis (or d-axis) current as an example to write the state equation, then the i_q's NESO in (15) can be expressed by

$$\begin{cases} e_\mathrm{q} = \hat{i}_\mathrm{q} - i_\mathrm{q} \\ \dot{\hat{i}}_\mathrm{q} = \hat{i}_\mathrm{qf} - \beta_1 e_\mathrm{q} + b v_\mathrm{q} \\ \dot{\hat{i}}_\mathrm{qf} = -\beta_2 f e_\mathrm{q} \\ y = i_\mathrm{q}. \end{cases} \tag{20}$$

After Laplace transformation (20), the transfer function expression of i_qf, i_q, and v_q can be obtained in

$$\hat{i}_\mathrm{qf}(s) = \beta_2 f \frac{i_\mathrm{q}(s)s - b v_\mathrm{q}(s)}{s^2 + s\beta_1 + \beta_2 f} \tag{21}$$

where, $i_\mathrm{q}(s)s - b v_\mathrm{q}(s) = i_\mathrm{qf}(s)$, then the above formula is shown in

$$\hat{i}_\mathrm{qf}(s) = \beta_2 f \frac{i_\mathrm{qf}(s)}{s^2 + s\beta_1 + \beta_2 f}. \tag{22}$$

The transfer function with i_qf as input and $\hat{i}_\mathrm{qf}$ as output is showing in

$$G(s) = \frac{\hat{i}_\mathrm{qf}(s)}{i_\mathrm{qf}(s)} = \frac{\beta_2 f}{s^2 + s\beta_1 + \beta_2 f}. \tag{23}$$

In (23), based on the Routh–Hurwitz criterion, it can be proven that the system is stable when $\beta_1 > 0, \beta_2 > 0$. Then, (23) is regarded as the second-order oscillation link (or low-pass filter)

$$G(s) = \frac{1}{\frac{s^2}{\omega_\mathrm{n}^2} + 2\xi\frac{s}{\omega_\mathrm{n}} + 1} \tag{24}$$

where $\omega_\mathrm{n} = \sqrt{\beta_2 f}, \xi = \frac{\beta_1}{2\sqrt{\beta_2 f}}$.

The oscillation frequency ω_n is defined as the observer bandwidth. The system damping is restricted to an overdamped range($\xi = 1$) to mitigate the amplification of high-frequency noise by the NESO. Defining the upper and lower bounds of f as f_max and f_min, the parameters of the observer can be determined as

$$\begin{cases} \beta_2 = \frac{\omega_\mathrm{n}^2}{f_\mathrm{min}} \\ \beta_1 = 2\xi\sqrt{\beta_2 f_\mathrm{max}} \end{cases}. \tag{25}$$

According to (19), the variation curve between f and the observed error is shown in Fig. 9(a) when $\alpha = 0.5$, $\delta = 0.01$.

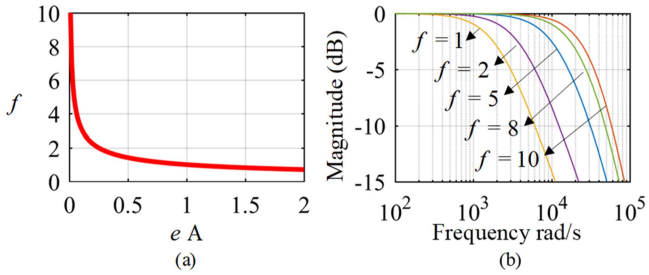

Fig. 9. NESO analysis. (a) Relationship between f and observation error e. (b) Logarithmic magnitude-frequency response curve of NESO.

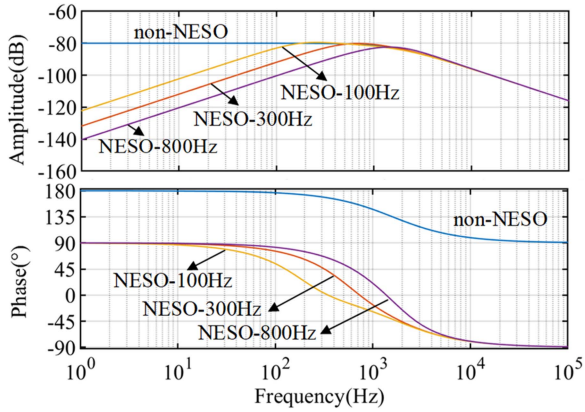

Fig. 10. Bode plot depicting the relationship between disturbance voltage and current.

The value of f solely depends on the system's steady-state error. Therefore, the range of f can be determined based on the system's error. For instance, considering the measurement noise of the system, with a maximum steady-state error of 1 and a minimum error of zero, according to Fig. 9(a), the range of f is determined to be 1 to 10. Therefore, $\beta_2 = \omega_\mathrm{n}^2$, $\beta_1 = 2\sqrt{10}\omega_\mathrm{n}$. The observation performance of the observer varies with the change in f when the bandwidth of the observer is set to 2000 rad/s, as shown in Fig. 9(b). It can be observed that regardless of the variation in f, the system's control requirements are met, and the observer exhibits accurate observation capability for disturbances.

According to Fig. 7 and the established NESO transfer function (23), the effect of system disturbances v_f on motor currents can be derived. The transfer function is as

$$\begin{aligned} \frac{v_\mathrm{f}(s)}{i_\mathrm{q}(s)} &= \frac{-T_\mathrm{s}s^2 + -T_\mathrm{s}\beta_1 s}{m_3\, s^3 + m_2 s^2 + m_1\, s + m_0} \\ m_3 &= L_\mathrm{s}T_\mathrm{s} \\ m_2 &= L_\mathrm{s} + R_\mathrm{s}T_\mathrm{s} + L_\mathrm{s}T_\mathrm{s}\beta_1 \\ m_1 &= L_\mathrm{s}\beta_1 + L_\mathrm{s}T_\mathrm{s}\beta_2 f + R_\mathrm{s}T_\mathrm{s}\beta_1 \\ m_0 &= L_\mathrm{s}\beta_2 f. \end{aligned} \tag{26}$$

As the bandwidth of NESO increases in Fig. 10, the system's disturbance rejection capability becomes stronger, indicating that NESO possesses robust disturbance suppression capability for the system.

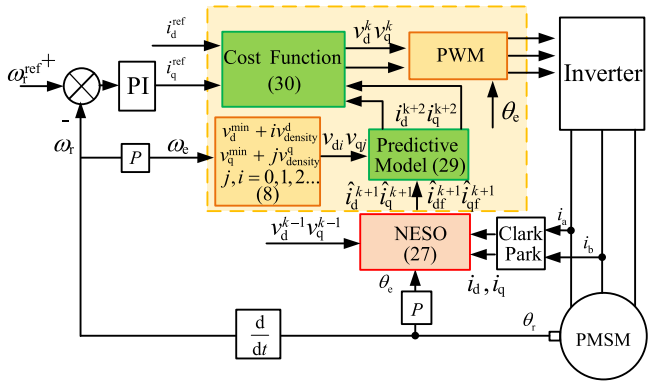

Fig. 11. Overall control block diagram of RACSMPCC.

C. RACSMPCC Based on NESO

After discretizing the NESO in (17) by the forward Euler method, the relevant variables at time $k+1$ can be obtained by

$$\begin{cases} \mathbf{e}_1^k = \mathbf{z}_1^k - \mathbf{i}_\mathrm{s}^k \\ \mathbf{z}_1^{k+1} = T_\mathrm{s}\mathbf{z}_2^k - T_\mathrm{s}\beta_1\mathbf{e}_1^k + T_\mathrm{s}b\mathbf{v}_\mathrm{s}^k + \mathbf{z}_1^k \\ \mathbf{z}_2^{k+1} = -T_\mathrm{s}\beta_2\mathrm{fal}(\mathbf{e}_1^k, \alpha, \delta) + \mathbf{z}_2^k \end{cases} \tag{27}$$

where

$$\mathbf{z}_1^{t+1} = \begin{bmatrix} \hat{i}_\mathrm{d}^{k+1} \\ \hat{i}_\mathrm{q}^{k+1} \end{bmatrix} \approx \mathbf{i}_\mathrm{s}^{k+1}, \mathbf{z}_2^{k+1} = \begin{bmatrix} \hat{i}_\mathrm{df}^{k+1} \\ \hat{i}_\mathrm{qf}^{k+1} \end{bmatrix} \approx \mathbf{i}_\mathrm{f}^{k+1}. \tag{28}$$

The disturbance and current values at $k+1$ can be predicted in (27) within k sampling periods. The implementation of delay compensation using NESO provides a convenient solution. Based on (14), the predictive equation is modified to

$$\begin{aligned} i_\mathrm{d}^{k+2} &= \hat{i}_\mathrm{d}^{k+1} + T_\mathrm{s}(bv_\mathrm{d}^k + \hat{i}_\mathrm{df}^{k+1}) \\ i_\mathrm{q}^{k+2} &= \hat{i}_\mathrm{q}^{k+2} + T_\mathrm{s}(bv_\mathrm{q}^k + \hat{i}_\mathrm{qf}^{k+1}). \end{aligned} \tag{29}$$

The RACSMPCC can be realized by the control set (8), prediction (29), and cost function

$$J_\mathrm{MPCC} = \left(i_\mathrm{d}^\mathrm{ref} - i_\mathrm{d}^{k+2}\right)^2 + \left(i_\mathrm{q}^\mathrm{ref} - i_\mathrm{q}^{k+2}\right)^2 + J_\mathrm{limit}. \tag{30}$$

D. Overall Control Block Diagram of RACSMPCC

Fig. 11 illustrates the overall control structure of RACSMPCC. After obtaining the sensor data, such as speed, dq-axis current information, and the previously recorded voltage control signal, the NESO is employed to observe the dq-axis current value and disturbance at $k+1$. These observed values are then used to construct the prediction equation. Subsequently, each control subset (8) is introduced to (29), allowing for predicting the dq-axis current of every subset at time $k+2$. The predicted value is compared with the current reference value calculated by the speed loop. Finally, the optimal control subset that minimizes the cost value is selected by (30). This optimal control subset corresponds to the control voltage, which is outputted through PWM to synthesize control vectors.

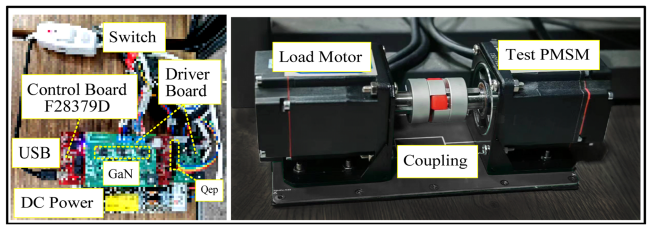

Fig. 12. Motor hardware structure diagram.

TABLE I
MOTOR PARAMETERS

Symbol	Parameters	Value
R_s	Phase resistance	0.22 Ω
L_s	Phase inductance	0.225 mH
P	Motor pole pairs	5
J	Moment of inertia	0.000023 Kg·m2
B	Viscous damping coefficient	0.3A/1000 rpm
i_N	Rated current	6 A
T_N	Rate torque	0.6 Nm
ω_N	Rated speed	2000 rpm
v_dc	Rated voltage	24 V

IV. Experimental Verification

An experimental hardware platform is built to verify the theoretical analysis in the previous parts, as shown in Fig. 12. In the platform, two SPMSMs are used for the drive motor and the load motor. The hardware parameters are shown in the Table I. The controller adopts the F28379D chip produced by TI. During the experiment, the internal data of DSP is uploaded to the host computer in real-time through serial communication. The switching frequency of 10 kHz is used in the experiment.

A. Experimental Results of ACSMPCC

First, the experiment compared the computation time of several mainstream methods: the PI controller, the original FCSMPCC, the TVMPCC [36] based on duty cycle calculation, the DCSMPCC [11] based on the expanded control set, and the ACSMPCC with NESO proposed in this article. A single-precision floating-point arithmetic was employed throughout the programming to maintain method fairness. Simultaneously, trigonometric functions are computed using a table lookup method, with efforts to optimize the associated computation process as much as possible. The experimental results are shown in Table II. The PI control method exhibits a distinct computational advantage due to its simple proportional and integral operations. The vector control set requires coordinate transformation during the prediction process, which involves significant trigonometric function computations. Despite optimizing the trigonometric function computations, the computational time for eight vector sets remains noticeably greater than that for fifteen amplitude subsets. Hence, the amplitude controller holds a significant advantage for processors with lower performance. In addition, Fig. 15(c) demonstrates that even fifteen amplitude

TABLE II
CALCULATION CYCLE COMPARISON

Test Type	Computation time (μs)
PI	17.3
FCSMPCC (8 Subsets)	26.5
TVMPCC (8 Subsets)	27.2
DCSMPCC (61 Subsets)	32.5
ACSMPCC (15 Subsets)	21.5
ACSMPCC (30 Subsets)	28.9
RACSMPCC with NESO (30 Subsets)	31.5

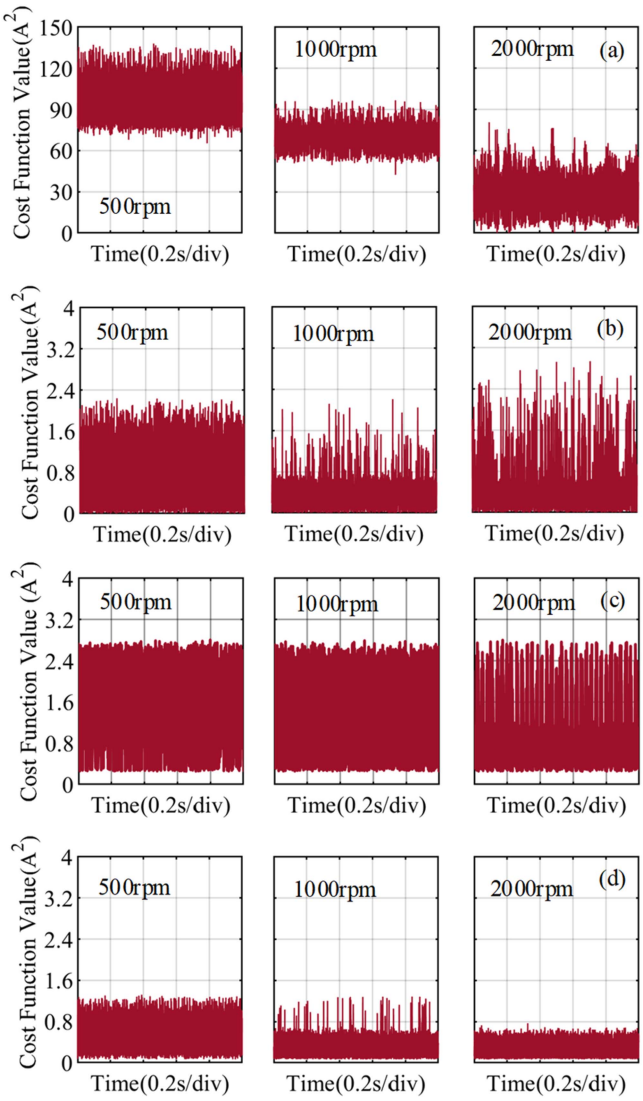

Fig. 15. Prediction error comparative analysis. (a) FCSMPCC. (b) DCSMPCC. (c) ACSMPCC (15 subsets). (d) ACSMPCC (30 subsets).

subsets have significantly lower cost values compared to FCSMPCC, illustrating the proposed method's high computational cost-effectiveness. For processors with superior performance, increasing the number of control sets can enhance steady-state control accuracy. Taking the F28379D controller in this article as an example, the maximum number of control subsets can

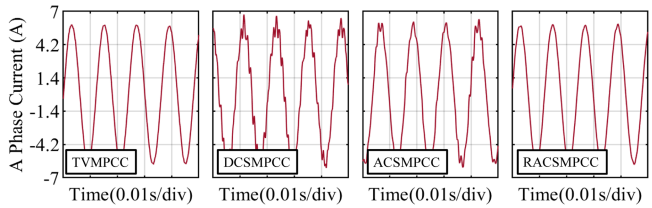

Fig. 13. Phase current comparative analysis between ACSMPCC and other methods.

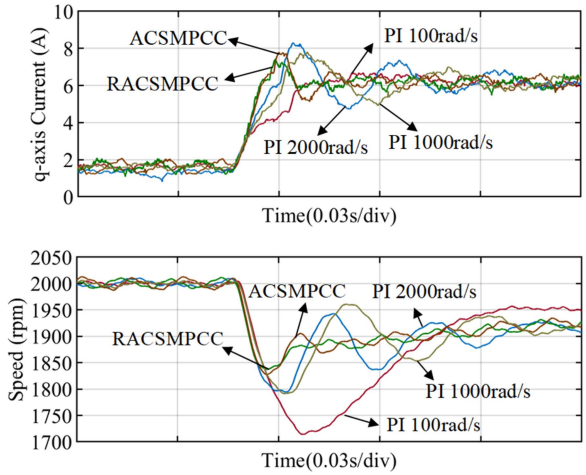

Fig. 14. Dynamic performance comparative analysis of ACSMPCC and PI control.

reach 60 (at a 10 kHz sampling frequency). However, 30 control sets were ultimately selected to facilitate communication, data transfer, and other functionalities. The number of control sets can be further reduced for motors with stronger filtering capabilities.

Fig. 13 shows the phase current of ACSMPCC, RACSMPCC, DCSMPCC, and TVMPCC. The torque in the experiment is set to rate torque. Due to the more accurate optimization of motor parameters in TVMPCC, the resulting output vector is improved, similar to ACSMPCC, exhibiting good performance in phase current. The phase current distortion is minimized, and the phase current is approximately sine. ACSMPCC introduces some parameter perturbations, resulting in certain current distortions. In contrast, DCSMPCC, despite having double the number of control sets compared to ACS-MPCC, exhibits notable current distortion resulting from errors in vector phase and amplitude. Experimental evidence of phase current distortion demonstrates the advantage of RACSMPCC in improving steady-state performance.

Fig. 14 tests the dynamic performance of the ACSMPCC compared to that of the PI to demonstrate that the amplitude control set does not affect the dynamic performance of the model predictive control. As the bandwidth of the current PI controller increases, the system's response becomes faster. However, this can lead to slight oscillations and harmonics, and further bandwidth increases can cause stability issues. In contrast, ACSMPCC, without parameter disturbance, or RACSMPCC, maintains a fast response speed with more minor oscillations than PI controllers.

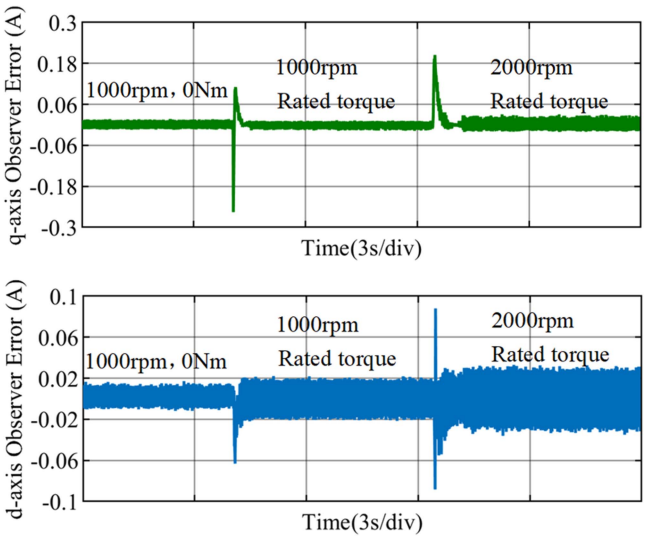

Fig. 16. Observation error in the dynamic process.

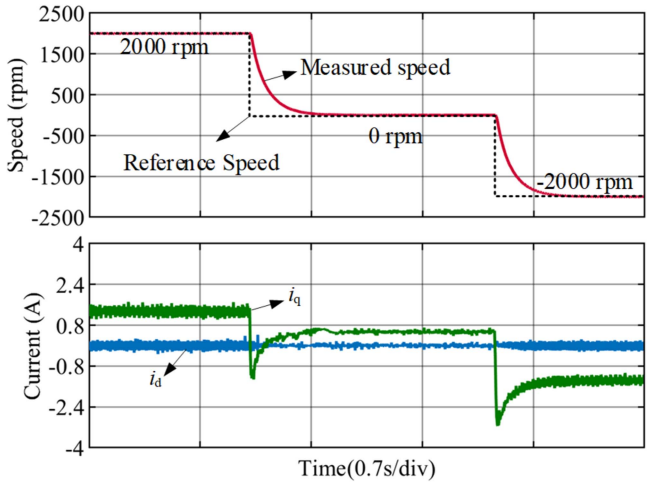

Fig. 17. Forward and reverse rotation test.

Fig. 15 compares FCSMPCC, DCSMPCC, and ACSMPCC prediction errors in 500 r/min, 1000 r/min, and 2000 r/min. FCSMPCC exhibits higher prediction errors across different operating conditions due to its utilization of only eight basic voltage vectors. DCSMPCC enhances the control accuracy of the control sets by constructing 61 virtual voltage vectors through configuring the duty cycle. However, each control solution still contains phase angle errors, resulting in a discrepancy in control accuracy compared to the amplitude control sets. The ACSMPCC is evaluated with both 15 and 30 subsets. It can be observed that employing 15 control subsets leads to a slight increase in the cost value compared to the case with 30 subsets. However, the configuration with 15 subsets still maintains an advantage over the FCSMPCC regarding prediction accuracy. TVMPCC achieves zero prediction error by directly optimizing the optimal control solution using the rate-of-change equation of the model and implementing duty cycle limiting.

The above experiments demonstrate that the ACSMPCC has good dynamic and steady-state performance. However, once subjected to parameter perturbations, the steady-state performance of the system will be reduced. The following will verify the antidisturbance performance of the NESO proposed in this article.

B. Experimental Results of RACSMPCC

First, the observed error of NESO is tested under different operating conditions. The steady-state error of the NESO is small, as depicted in Fig. 16, indicating high accuracy in observation under various operating conditions.

The RACSMPCC was tested for forward and reverse rotations, as shown in Fig. 17. The steady-state current on the d-axis is around 0 A, and the motor efficiency is relatively high. Due to the influence of frictional resistance, there is a certain amount of q-axis current, and it exhibits symmetry in both forward and reverse operating conditions. The experimental results demonstrated that the motor speed can be effectively controlled within the rated speed range (±2000 r/min).

In RACSMPCC, a single motor-related parameter, denoted as b in (29), is utilized. Although this value is a proportional coefficient in the super-local model, setting b equal to $1/L_s$ is more appropriate to ensure consistency between the predictive and the actual motor equation. The motor inductance decreases usually as the load increases [37]. Therefore, the system's performance was tested when this value varied in Fig. 18. The inductance parameter in the control program was adjusted to conduct the experiments. In Fig. 18(a), parameter b undergoes a step change in the range of 0.5 to 5, which tests the extreme situation of motor state variations. Although the motor has experienced current and speed spikes, the system converged quickly, indicating high robustness. The control system exhibits lower sensitivity to variations in larger inductance values than smaller inductance values. In Fig. 18(b), the different b values affected the system's dynamic performance. Since b influences the control gain of the current, a higher gain leads to a faster current response and better speed performance. Therefore, when designing the system, choosing a slightly larger value than the actual value ($1/L_s$) for b is advantageous as it is more conducive to control.

Fig. 19 presents the results of the current tracking experiment for RACSMPCC in both rotating and stationary coordinate systems. The reference and actual values of the current are in close agreement, indicating that the current prediction equation based on NESO exhibits high accuracy.

Then, sinusoidal disturbances (The amplitudes are 5% of v_{dc}, and the frequency is 10 Hz, 50 Hz, and 100 Hz) were intentionally added to the voltage loop of the motor to test the disturbance rejection capabilities of TVMPCC, DCSMPCC, and RACSMPCC. The experimental results are shown in Figs. 20 and 21. In Fig. 20(a), when there is no disturbance in the system, TVMPCC achieves a cost deviation of zero by sacrificing multiobjective optimization, resulting in the lowest ripple in q-axis current and speed. RACSMPCC also exhibits strong ripple suppression in current. However, when disturbances are present in the system in Fig. 20(a), TVMPCC and DCSMPCC represent

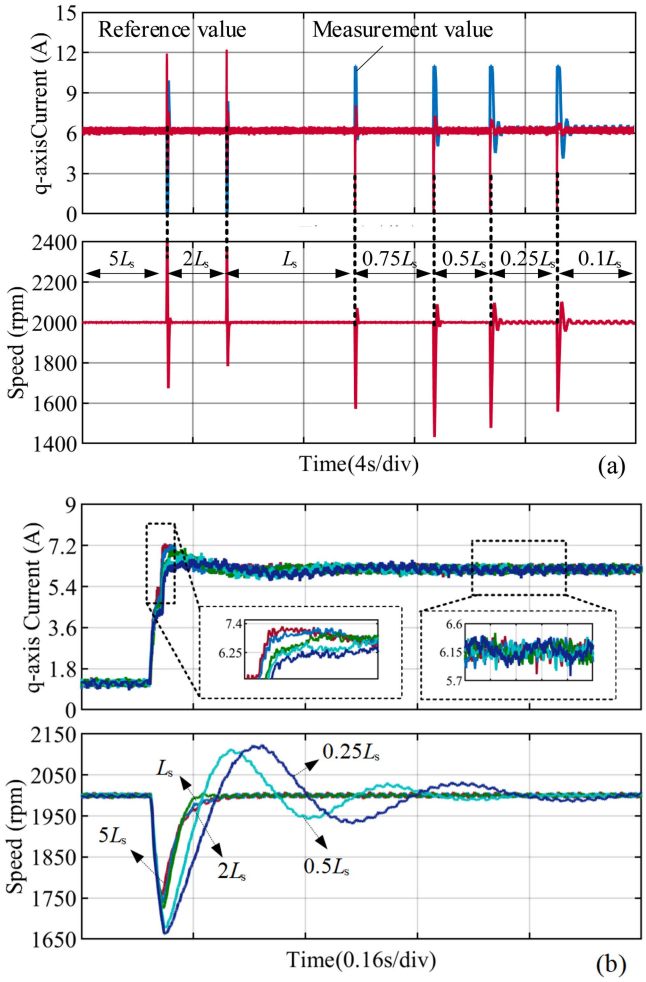

Fig. 18. Experimental results of time-varying parameters. (a) Steady-state performance test. (b) Dynamic performance test.

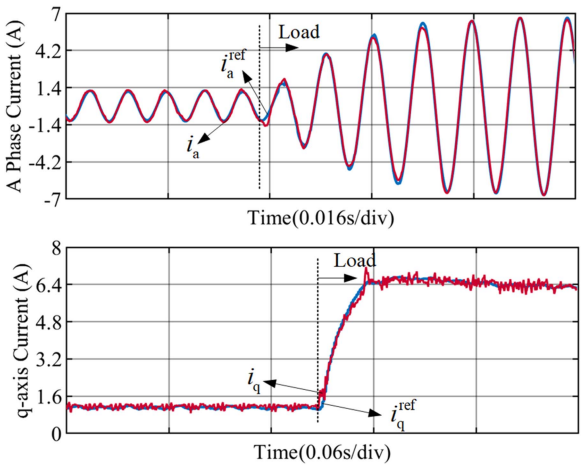

Fig. 19. Current tracking performance during dynamic processes.

more significant amplitude speeds and current ripples, while RACSMPCC exhibits the lowest. The specific harmonic content can be seen in Fig. 21. In the absence of disturbance, there is little difference in the harmonic content between RACSMPCC and TVMPCC. However, when disturbances are present, the

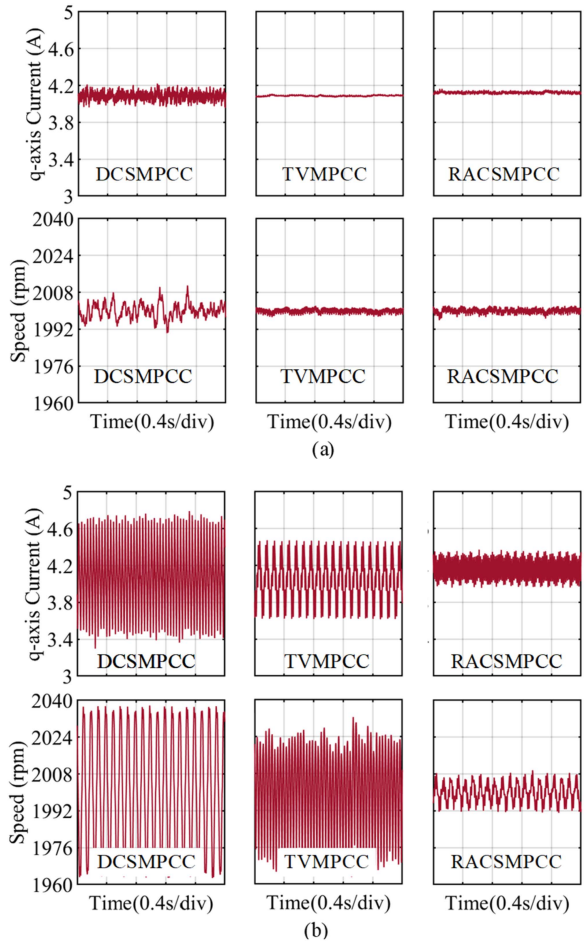

Fig. 20. Results of disturbance rejection experiment of different control methods. (a) Without disturbances. (b) With the disturbances.

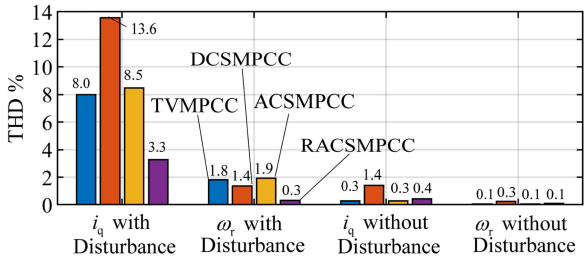

Fig. 21. Harmonic contrast analysis in the presence of parameter disturbance.

advantage of RACSMPCC becomes apparent as it exhibits more robust disturbance rejection capabilities. Results of the disturbance experiment indicate that RACSMPCC has more vital disturbance rejection capabilities.

To further validate the advantages of NESO, Fig. 22 presents experimental comparisons of the sliding mode observer (SMO) [27] and the Luenberger disturbance observer (LDO) [25]. SMO shows superior dynamic performance but struggles with parameter tuning from a bandwidth perspective due to its large number of parameters. Consequently, it exhibits poorer noise suppression ability and more pronounced current overshoot. On the other hand, NESO allows for flexible bandwidth configuration, enabling a more accessible selection of optimal control

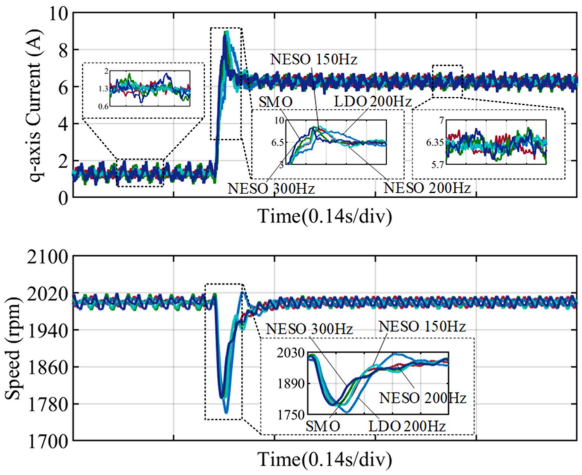

Fig. 22. Experimental results of different disturbance observers.

parameters for the system. Its dynamic performance surpasses that of SMO in high-bandwidth applications. However, LDO's current dynamic performance and speed disturbance rejection capability are inferior to the other two methods due to the absence of a high-gain stage. Considering all these factors, NESO performs better in both rapid and steady-state behavior, making it a more favorable choice for system control.

Based on the experimental results, it is evident that RAC-SMPCC exhibits superior dynamic performance compared to proportional-integral controllers. It effectively reduces current harmonics and enhances computational efficiency compared to the vector extended set by minimizing the cost function value. Moreover, using NESO for predictive equation compensation dramatically improves the system's disturbance rejection capabilities.

V. Conclusion

This study presents a novel approach to enhance the steady-state performance of SPMSMs by introducing an RACSMPCC based on the NESO. The proposed method mitigates steady-state current harmonics caused by predictive errors and unknown disturbances. An amplitude control set is designed based on an analysis of the motor voltage equation to improve control accuracy and computation efficiency. By utilizing the NESO, current disturbances can be effectively observed and minimized, thereby reducing the impact of motor parameter variations on steady-state performance. In addition, the influence of NESO on the system's disturbance rejection capability is investigated. Experimental validation is conducted on a test platform to evaluate the effectiveness of RACSMPCC, and comparative studies demonstrate its superior performance in terms of current dynamic performance and harmonic suppression.

References

[1] Z. Zhang, M. Luo, J.-A. Duan, and B. Kou, "Design and analysis of a novel frequency modulation secondary for high-speed permanent magnet linear synchronous motor," *IEEE/ASME Trans. Mechatron.*, vol. 27, no. 2, pp. 790–799, Apr. 2022.

[2] X. Yang, X. Wang, S. Wang, K. Wang, and M. B. Sial, "Finite-time adaptive dynamic surface synchronization control for dual-motor servo systems with backlash and time-varying uncertainties," *Instrum. Soc. Amer. Trans.*, vol. 137, pp. 248–262, Jun. 2023.

[3] Y. Gao, M. Doppelbauer, J. Ou, and R. Qu, "Design of a double-side flux modulation permanent magnet machine for servo application," *IEEE J. Emerg. Sel. Topics Power Electron.*, vol. 10, no. 2, pp. 1671–1682, Apr. 2022.

[4] A. G. Yepes, A. Vidal, J. Malvar, O. López, and J. Doval-Gandoy, "Tuning method aimed at optimized settling time and overshoot for synchronous proportional-integral current control in electric machines," *IEEE Trans. Power Electron.*, vol. 29, no. 6, pp. 3041–3054, Jun. 2014.

[5] L. Zhong, M. F. Rahman, W. Y. Hu, and K. W. Lim, "Analysis of direct torque control in permanent magnet synchronous motor drives," *IEEE Trans. Power Electron.*, vol. 12, no. 3, pp. 528–536, May 1997.

[6] W. Tu, G. Luo, Z. Chen, L. Cui, and R. Kennel, "Predictive cascaded speed and current control for PMSM drives with multi-timescale optimization," *IEEE Trans. Power Electron.*, vol. 34, no. 11, pp. 11046–11061, Nov. 2019.

[7] M. Preindl and S. Bolognani, "Model predictive direct torque control with finite control set for PMSM drive systems, part 1: Maximum torque per ampere operation," *IEEE Trans. Ind. Inform.*, vol. 9, no. 4, pp. 1912–1921, Nov. 2013.

[8] Y. Zhang, X. Liu, and H. Yang, "Relationship between finite control set model predictive control and direct current control with duty ratio optimization for power converters," in *Proc. 22nd Int. Conf. Elect. Mach. Syst.*, 2019, pp. 1–6.

[9] M. Preindl and S. Bolognani, "Model predictive direct torque control with finite control set for PMSM drive systems, part 2: Field weakening operation," *IEEE Trans. Ind. Inform.*, vol. 9, no. 2, pp. 648–657, May 2013.

[10] T. Dragičević, "Dynamic stabilization of DC microgrids with predictive control of point-of-load converters," *IEEE Trans. Power Electron.*, vol. 33, no. 12, pp. 10872–10884, Dec. 2018.

[11] M. Xiao, T. Shi, X. Gu, and C. Xia, "Simplified predictive torque control for permanent magnet synchronous motor with discrete duty cycle control," *Inst. Eng. Technol. Electric Power Appl.*, vol. 13, no. 3, pp. 294–301, Mar. 2019.

[12] X. Zhang, L. Zhang, and Y. Zhang, "Model predictive current control for PMSM drives with parameter robustness improvement," *IEEE Trans. Power Electron.*, vol. 34, no. 2, pp. 1645–1657, Feb. 2019.

[13] M. H. Vafaie, B. M. Dehkordi, P. Moallem, and A. Kiyoumarsi, "A new predictive direct torque control method for improving both steady-state and transient-state operations of the PMSM," *IEEE Trans. Power Electron.*, vol. 31, no. 5, pp. 3738–3753, May 2016.

[14] X. Zhang and Y. He, "Robust model predictive direct speed control for SPMSM drives based on full parameters and load observer," in *Proc. IEEE Int. Symp. Predictive Control Elect. Drives Power Electron.*, 2019, pp. 1–5.

[15] Y. Liu, S. Cheng, Y. Zhao, J. Liu, and Y. Li, "Optimal two-vector combination-based model predictive current control with compensation for PMSM drives," *Int. J. Electron.*, vol. 106, no. 6, pp. 880–894, Jun. 2019.

[16] V. P. Muddineni, S. R. Sandepudi, and A. K. Bonala, "Finite control set predictive torque control for induction motor drive with simplified weighting factor selection using TOPSIS method," *Inst. Eng. Technol. Electric Power Appl.*, vol. 11, no. 5, pp. 749–760, May 2017.

[17] Y. Wang et al., "Deadbeat model-predictive torque control with discrete space-vector modulation for PMSM drives," *IEEE Trans. Ind. Electron.*, vol. 64, no. 5, pp. 3537–3547, May 2017.

[18] T. Wang, C. Liu, G. Lei, Y. Guo, and J. Zhu, "Model predictive direct torque control of permanent magnet synchronous motors with extended set of voltage space vectors," *Inst. Eng. Technol. Electric Power Appl.*, vol. 11, no. 8, pp. 1376–1382, Sep. 2017.

[19] Z. Zhou, C. Xia, Y. Yan, Z. Wang, and T. Shi, "Torque ripple minimization of predictive torque control for PMSM with extended control set," *IEEE Trans. Ind. Electron.*, vol. 64, no. 9, pp. 6930–6939, Sep. 2017.

[20] X. Song, H. Wang, X. Ma, X. Yuan, and X. Wu, "Robust model predictive current control for a nine-phase open-end winding PMSM with high computational efficiency," *IEEE Trans. Power Electron.*, vol. 38, no. 11, pp. 13933–13943, Nov. 2023.

[21] X. Liu, S. Lou, and W. Dai, "Further results on 'system identification of nonlinear state-space models," *Automatica J. Int. Federation Autom. Control*, vol. 148, Feb. 2023, Art. no. 110760.

[22] M. Siami, D. A. Khaburi, A. Abbaszadeh, and J. Rodriguez, "Robustness improvement of predictive current control using prediction error correction for permanent-magnet synchronous machines," *IEEE Trans. Ind. Electron.*, vol. 63, no. 6, pp. 3458–3466, Jun. 2016.

[23] J.-F. Stumper, S. Kuehl, and R. Kennel, "Predictive torque control for AC drives: Improvement of parametric robustness using two-degree-of-freedom control," in *Proc. IEEE Energy Convers. Congr. Expo.*, 2013, pp. 1170–1175.
[24] Z. Chen, J. Qiu, and M. Jin, "Prediction-error-driven position estimation method for finite-control-set model predictive control of interior permanent-magnet synchronous motors," *IEEE J. Emerg. Sel. Topics Power Electron.*, vol. 7, no. 1, pp. 282–295, Mar. 2019.
[25] L. He, F. Wang, J. Wang, and J. Rodríguez, "Zynq implemented luenberger disturbance observer based predictive control scheme for PMSM drives," *IEEE Trans. Power Electron.*, vol. 35, no. 2, pp. 1770–1778, Feb. 2020.
[26] F. Mwasilu, H. T. Nguyen, H. H. Choi, and J.-W. Jung, "Finite set model predictive control of interior PM synchronous motor drives with an external disturbance rejection technique," *IEEE/ASME Trans. Mechatron.*, vol. 22, no. 2, pp. 762–773, Apr. 2017.
[27] L. He, F. Wang, and D. Ke, "FPGA-based sliding-mode predictive control for PMSM speed regulation system using an adaptive ultralocal model," *IEEE Trans. Power Electron.*, vol. 36, no. 5, pp. 5784–5793, May 2021.
[28] Y. A.-R. I. Mohamed, "Design and implementation of a robust current-control scheme for a PMSM vector drive with a simple adaptive disturbance observer," *IEEE Trans. Ind. Electron.*, vol. 54, no. 4, pp. 1981–1988, Aug. 2007.
[29] Y. Lu, C. Tan, W. Ge, Y. Zhao, and G. Wang, "Adaptive disturbance observer-based improved super-twisting sliding mode control for electromagnetic direct-drive pump," *Smart Mater. Struct.*, vol. 32, no. 1, Jan. 2023, Art. no. 17001.
[30] J. Han, "From PID to active disturbance rejection control," *IEEE Trans. Ind. Electron.*, vol. 56, no. 3, pp. 900–906, Mar. 2009.
[31] Y. Zhang, J. Jin, and L. Huang, "Model-free predictive current control of PMSM drives based on extended state observer using ultralocal model," *IEEE Trans. Ind. Electron.*, vol. 68, no. 2, pp. 993–1003, Feb. 2021.
[32] A. H. M. Sayem, Z. Cao, and Z. Man, "Model free ESO-based repetitive control for rejecting periodic and aperiodic disturbances," *IEEE Trans. Ind. Electron.*, vol. 64, no. 4, pp. 3433–3441, Apr. 2017.
[33] L. Wang, S. Chai, D. Yoo, L. Gan, and K. Ng, "FCS predictive control in - reference frame," in *PID and Predictive Control of Electrical Drives and Power Converters using MATLAB / Simulink*, 2015, ch. 6, pp. 171–235, doi: 10.1002/9781118339459.
[34] Z. Gao, Y. Huang, and J. Han, "An alternative paradigm for control system design," in *Proc. IEEE 40th Conf. Decis. Control*, 2001, vol. 5, pp. 4578–4585.
[35] J. Li, Y. Xia, X. Qi, and Z. Gao, "On the necessity, scheme, and basis of the linear–nonlinear switching in active disturbance rejection control," *IEEE Trans. Ind. Electron.*, vol. 64, no. 2, pp. 1425–1435, Feb. 2017.
[36] J. Ji, R. Xue, W. Zhao, T. Tao, and L. Huang, "Simplified three-vector-based model predictive thrust force control with cascaded optimization process for a double-side linear vernier permanent magnet motor," *IEEE Trans. Power Electron.*, vol. 35, no. 10, pp. 10681–10689, Oct. 2020.
[37] P. Phowanna, S. Boonto, and M. Konghirun, "Online parameter identification method for IPMSM drive with MTPA," in *Proc. 18th Int. Conf. Elect. Mach. Syst.*, 2015, pp. 1775–1780.

Zhenrui Zhang born in Qingdao, China, in 1994. He received the bachelor's degree in engineering from Yantai University, Yantai, China, in 2017, and the master's and Ph.D. degrees in engineering from Dalian Maritime University, Dalian, China, From 2017 to 2023.

He is a Full-Time Researcher with the Institute of Marine Equipment and Technology, Jiangsu University of Science and Technology, Zhenjiang, China. His research interests include permanent magnet synchronous motor drive control, model predictive control, thin film capacitor drive systems, and shipborne electric propulsion systems.

Xingyu Wang was born in Jinzhou City, China, in 1989. He received the B.S. degree in electrical engineering and automation and the M.S. degree in electrical engineering from Liaoning University of Engineering and Technology, Jinzhou City, China, in 2014 and 2017, respectively, and the Ph.D. degree in power electronics and electric drive from Northeastern University, Liaoning, China, in 2022.

He is currently with the Marine Equipment and Technology Institute, Jiangsu University of Science and Technology, Jiangsu, China. His research interests include robotic manipulator motion control, servo drive system, Intelligent manufacturing, sliding electrical contact, and basic theory of electrical equipment.

Jing Xu received the Ph.D. degree in mechatronic engineering from China University of Mining and Technology, Xuzhou, China, in 2018.

He is an Associate Professor of mechatronic engineering with Marine Equipment and Technology Institute, Jiangsu University of Science and Technology, Zhenjiang, China. His research interests include signal processing, pattern recognition, and intelligent system.